J. Plasma Phys. (2024), *vol.* 90, 905900603

Published by Cambridge University Press

doi:10.1017/S0022377824000552

Plasma potential shaping using end-electrodes in the Large Plasma Device

R. Gueroult[1],†, **S.K.P. Tripathi**[2], **F. Gaboriau**[1], **T.R. Look**[2] and **N.J. Fisch**[3]

[1]LAPLACE, Université de Toulouse, CNRS, INPT, UPS, 31062 Toulouse, France

[2]Department of Physics and Astronomy, University of California, Los Angeles, CA 90095, USA

[3]Department of Astrophysical Sciences, Princeton University, Princeton NJ 08540, USA

(Received 12 January 2024; revised 5 April 2024; accepted 5 April 2024)

We perform experiments in the Large Plasma Device at the University of California, Los Angeles, studying how different end-electrode biasing schemes modify the radial potential profile in the machine. We impose biasing profiles of different polarities and gradient signs on a set of five concentric electrodes placed 12 m downstream from the plasma source. We find that imposing concave-down profiles (negative potential radial gradient) on the electrodes creates radial potential profiles halfway up the plasma column that are comparable to those imposed on the electrodes and a few electron temperature in height, regardless of the biasing polarity. On the other hand, imposing concave-up profiles (positive potential radial gradient) leads to non-monotonic radial potential profiles. This observation can be explained by the current drawn through the electrodes and the parallel plasma resistivity, highlighting their important role in controlling the rotation of plasma. Concave-down plasma potential profiles, obtained by drawing electrons on the axis, are predicted to drive azimuthal drift velocities that can approach significant fractions of the ion sound speed in the central region of the plasma column.

Keywords: plasma dynamics, plasma flows, plasma applications

1. Introduction

Producing and controlling rotation in plasmas is attractive for a number of applications (Lehnert 1971). For example, plasma rotation could prove essential for advancing magnetic confinement fusion in both linear (Ellis *et al.* 2001, 2005; Romero-Talamás *et al.* 2021; Endrizzi *et al.* 2023) and toroidal (Rax, Gueroult & Fisch 2017) geometries. Plasma rotation control is also a key element in advancing plasma mass separation technologies (Gueroult *et al.* 2018; Zweben, Gueroult & Fisch 2018), both in plasma centrifuges for isotope separation (Krishnan, Geva & Hirshfield 1981; Fetterman & Fisch 2009; Borisevich, Potanin & Whichello 2020) and cross-field rotating collisionless separator concepts targeting new separation needs (Ohkawa & Miller 2002; Fetterman & Fisch 2011; Gueroult, Rax & Fisch 2014; Liziakin *et al.* 2022). Finally, controlling plasma rotation in

---

† Email address for correspondence: renaud.gueroult@laplace.univ-tlse.fr

laboratory experiments provides unique opportunities for investigating the role of plasma rotation in affecting the dynamics of laboratory and space plasmas – such as the formation of accretion disks (Flanagan *et al.* 2020; Valenzuela-Villaseca *et al.* 2023) and propagation characteristics of plasma waves (Gueroult *et al.* 2019*b*; Gueroult, Rax & Fisch 2023).

In magnetised plasmas, a possible means of controlling rotation is through cross-field drift driven by a perpendicular electric field. While new promising schemes harnessing beams and waves have been proposed to establish this perpendicular electric field (Putvinskii 1981; Rax, Gueroult & Fisch 2023), a long-studied solution is to use biased electrodes. One option is to bias electrodes positioned at the outer edge of the plasma, referred to as limiters, to impose a radial potential difference. Although this scheme has been shown to effectively establish an electric field and rotation in the plasma edge (Schaffner *et al.* 2012), the electric field and rotation in the bulk plasma is due to plasma self-reorganisation (Weynants & Oost 1993) and cannot be directly controlled. Another option, which has been surmised to provide greater control over the electric field in the plasma bulk, is the end-electrodes scheme originally proposed by Lehnert (1970, 1973). The principle is to use independently biased electrodes, on which the plasma column terminates, to finely shape the perpendicular electric field in the plasma bulk. Despite having been implemented in numerous experimental set-ups over the years (see e.g. Gueroult *et al.* (2019*c*) and references therein), the effectiveness of end-electrode biasing in controlling the perpendicular electric field across plasma regimes remains unclear. Two outstanding issues are determining the fraction of the imposed bias lost in the sheath and how much the potential varies along magnetic field lines (Trotabas & Gueroult 2022). In this study, we report the results of an experimental campaign using end-electrodes carried out in the Large Plasma Device (LAPD) at the University of California, Los Angeles in August 2023 that shed light on this problem.

As mentioned above, numerous experiments have used biased end-electrodes. However, the operating conditions and size of LAPD allow for exploring different regimes. Indeed, it has been shown (Gueroult, Rax & Fisch 2019*a*; Poulos 2019) that an important dimensionless parameter affecting the uniformity of the plasma potential along a field line is

$$\tau = \frac{L}{a}\sqrt{\frac{\sigma_\perp}{\sigma_\parallel}} \tag{1.1}$$

with L and a the plasma column length and radius, respectively, and $\sigma_\perp$ and $\sigma_\parallel$ the perpendicular and parallel plasma conductivities. Many of the recent end-electrodes biasing experiments used helicon plasmas in midsize experiments where typically $\tau \geq 1$ (Gilmore *et al.* 2011, 2014; Zhang *et al.* 2015; Gueroult *et al.* 2016; Liziakin *et al.* 2019; Désangles *et al.* 2021). However, this regime has been inferred to prohibit effective electrical connection between symmetrical electrodes positioned at opposite ends of the machine (Gueroult *et al.* 2019*a*), contrary to the operating principle envisioned by Lehnert (1970, 1973). On the other hand the low operating pressure in LAPD typically leads to regimes where $\tau \ll 1$, creating opportunities to test these models.

This paper is organised as follows. In § 2 we begin by introducing the experimental set-up used in this experimental campaign, and how it both relates to and differs from past experiments. In § 3 we analyse plasma parameter profiles obtained for the selected operating condition prior to inserting the electrodes in the machine, which will serve as a baseline. In § 4 we present results obtained for a set of six complementary biasing scenarios, which are shown to exhibit distinctly different plasma potential profiles. In § 5 we then propose a simple analysis to explain trends in plasma potential modifications, considering both the voltage drop along field lines and the dynamics of the anode–plasma system, and discuss this model in light of previous contributions. Finally, in § 6 we use the plasma potential profiles measured in the different biasing scenarios to infer the corresponding plasma rotation expected from cross-field drift and show how imposing a concave-down biasing profile leads to azimuthal drift velocities approaching a significant fraction of the ion sound speed. These results are briefly discussed in regard to previous studies demonstrating biasing driven rotation in LAPD. Lastly, in § 7, we summarise the main findings of this study.

2. Experimental set-up

In this section, we introduce the main characteristics of the experimental set-up used in this campaign, which will be helpful for our upcoming analysis and discussion of biasing results.

2.1. *Biasing set-up*

Experiments are carried out in the LAPD at the University of California, Los Angeles (Gekelman *et al.* 2016). The LAPD uses a large 38-cm-diameter hot LaB_6 cathode (Qian *et al.* 2023) to produce a highly reproducible 20 m long, 75-cm-diameter magnetised plasma column with a repetition rate of 0.3–1 Hz.

In this campaign, we use a set of five stainless steel disks, electrically separated by ceramic spacers, to form a stack of concentric electrodes as shown in figure 1(*a*). Each disk, $\mathcal{E}_i$ with $i \in [\![1, 5]\!]$, has a radius $r_i = 2.54i$ cm. This electrode stack, or multidisk electrode, is centred radially at the machine port #35 and rotated perpendicular to the magnetic field. As illustrated in figure 2, the electrode stack is approximately 11 m from the anode. Although this multidisk electrode set-up is similar in design and comparable in size to one previously used in LAPD by Koepke *et al.* (2008, 2016), an important difference concerns the biasing scheme on the electrodes. In this study, we bias each electrode with respect to the machine ground, whereas electrodes were biased with respect to each other (or a group with respect to another group) in earlier studies. As highlighted in figure 1(*b*), the voltage ϕ_i of each electrode $\mathcal{E}_i$ is set by positioning pins across a resistive voltage divider ($R_d \sim 1.1\ \Omega$), which is connected to a capacitor bank through a transistor switch. We note that this experimental set-up also shares commonalities with the work by Jin *et al.* (2019), though in this case, the emissive cathode positioned in the machine was biased with respect to the anode.

We also note an important difference in this set-up compared with the canonical end-electrodes configuration proposed by Lehnert (1970). As shown in figure 2, one end of the machine is blocked by the anode mesh. As a result, the configuration is not symmetrical. Although it makes it impossible to test the assumption of effective electrical connection between symmetrical end-electrodes for $\tau \ll 1$, it is still possible to study how the potential distributes itself along and across field lines in these conditions. In this regard, our study builds on the study by Jin *et al.* (2019) by exploring different biasing configurations using multiple electrodes ϕ_i and both positive and negative biases.

2.2. *Shot parameters*

With the LAPD cathode upgrade (Qian *et al.* 2023), the discharge is fuelled by gas puffed near the new LaB_6 source. In this campaign, we use a helium gas puff with a maximum chamber pressure reaching 3.45×10^{-5} Torr and a 15-ms-long pulsed discharge with a repetition rate of 1 Hz. The source magnetic field and magnetic field in the main chamber are, respectively, $B_s = 0.2$ T and $B_0 = 0.1$ T, for a field ratio $\rho_B \doteq B_s/B_0 = 2$. In these conditions, as can be seen in figure 3, the peak discharge current is $I_d \sim 3.2$ kA with an anode–cathode voltage difference of approximately 65 V. We will verify that it

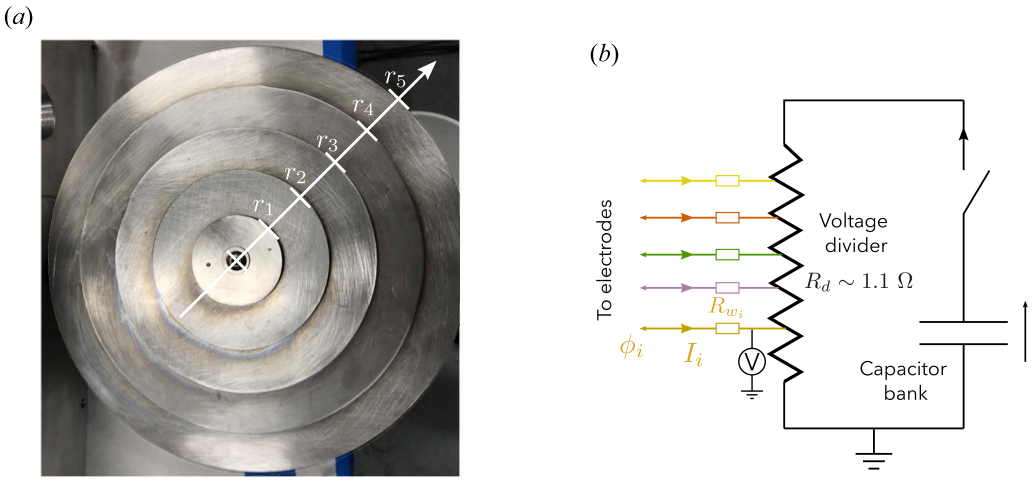

FIGURE 1. Picture of the multidisk electrode used in this experimental campaign (*a*) and electric circuit used to bias each electrode (*b*). The outer radius of each electrode is $r_i = 2.54i$ cm, $i \in [\![1, 5]\!]$. Here R_{w_i} is the resistance of the cable between the point of measure near the voltage divider and the disk $\mathcal{E}_i$ in the machine.

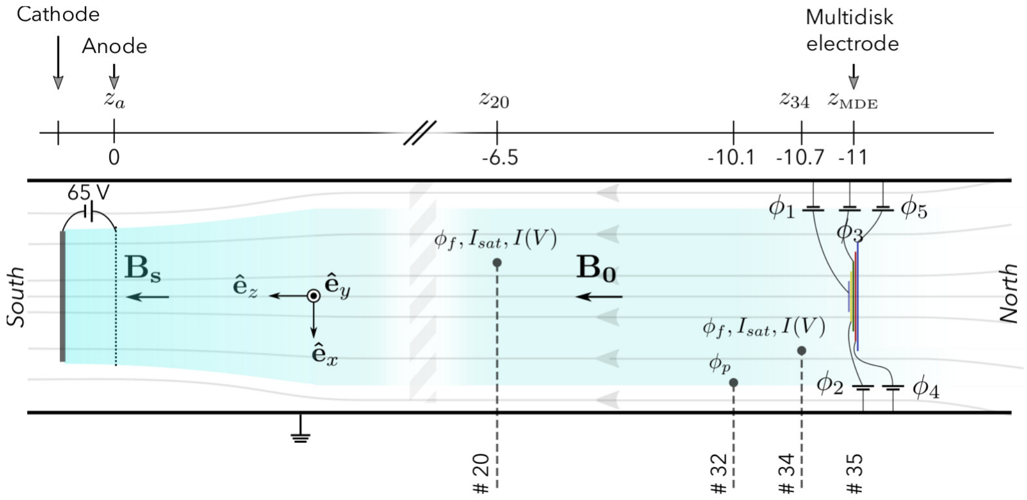

FIGURE 2. Experimental set-up used in this campaign. The plasma is created by applying a voltage between the cathode and a mesh anode. The five concentric disk electrodes are installed on port #35 and biased with respect to the grounded vacuum chamber, with bias ϕ_i for $i \in [\![1, 5]\!]$. The magnetic field in the source B_s is 0.2 T whereas the field in the main chamber B_0 is 0.1 T.

corresponds to a plasma density of approximately $6 \times 10^{18}\ \mathrm{m}^{-3}$, which was used as our target operating point during the one-week-long campaign.

The active phase during which electrodes are biased starts at 12 ms and ends at 18 ms (blue region in figure 3). The active bias phase thus covers both the end of the main discharge during which electrons are still injected in the plasma and the afterglow regime which refers to the phase after the discharge voltage has been switched off (Gekelman

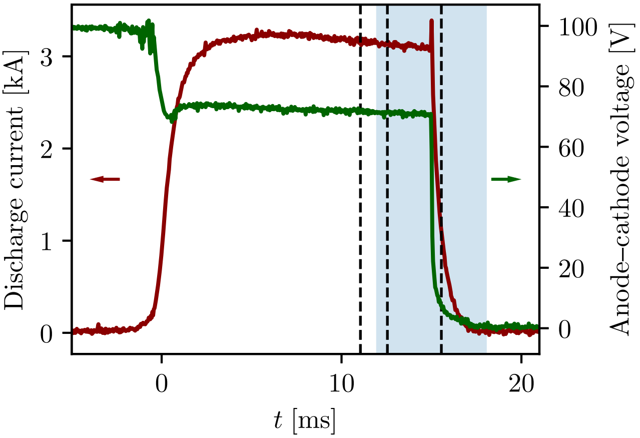

FIGURE 3. Time evolution of the anode–cathode voltage (green, right-hand axis) and discharge current (red, left-hand axis) during a typical shot. The $t = 0$ reference corresponds to $I_d = 1$ kA. The blue region $12 \leq t \leq 18$ ms corresponds to the time the electrode bias is on. The vertical dashed lines indicate three different instants during the shot that we will focus on in our data analysis. The first one (11.1 ms) is before bias has been turned on, the second one (12.6 ms) is during the main discharge with bias on, and the last one (15.6 ms) is in the afterglow with bias on.

et al. 2016). Since the electron temperature T_e drops rapidly in the afterglow, this allows probing the effect of biasing in different plasma conditions.

2.3. *Diagnostics*

Plasma parameters in the machine are inferred through a suite of probe diagnostics. In this campaign, four-tip probes are mounted on probe drives on ports #20 and #34, which correspond to distances of approximately 5.5 m and 30 cm from the multidisk electrode. The tip area is approximately 4 mm^2. On each of these probes, three tips are used. Two of these three tips are used to acquire, respectively, the ion saturation current I_{sat} and the floating potential ϕ_f. The last tip is used as a swept Langmuir probe to acquire $I(V)$ characteristics. Plasma potential estimates ϕ_p are obtained from $I(V)$ probe characteristics using spline fitting and a standard inflection-point method (Godyak & Alexandrovich 2015). The electron temperature is determined from a linear fit of the logarithm of the electron current as a function of bias for biases between the floating potential and the inflection point. Practically, 200-ms-long $I(V)$ Langmuir sweeps separated by a 100 ms pause were used, for a total of 23 sweeps starting at $t = 11.1$ ms. In addition, an emissive probe (Martin *et al.* 2015) is mounted on a third probe drive on port #32, which is approximately 90 cm away from the multidisk electrode. The heating current is first adjusted to ensure symmetrical $I(V)$ curves, whereafter the plasma potential ϕ_p is taken to be the floating potential of the emissive electrode. All three probe drives are computer-controlled, making it possible to obtain two-dimensional maps of plasma parameters at three axial locations (ports #20, #32 and #34). In practice we will mostly focus on results from planes at ports #20 and #34, and will verify that the plasma potential estimated from the emissive probe on port #32 is consistent with estimates obtained from $I(V)$ data on port #34. Absolute plasma density estimates are simply deduced from I_{sat} data after calibration using microwave interferometric data taken on port #20. Variations in I_{sat} are therefore entirely attributed to variations in density n, while they could also result from variations in electron temperature T_e. Although crude, this assumption is supported by the weaker dependence of the ion saturation on the temperature ($\propto\sqrt{T_e}$) compared with the density ($\propto n_e$), and the relatively limited variations in T_e which will be observed. Lastly, the data presented here is averaged over five shots taken at the same spatial position, with error bars quantifying the standard deviation over these five shots.

Besides plasma parameters and general machine parameters, the voltage ϕ_i of each electrode $\mathcal{E}_i$ with $i \in [\![1, 5]\!]$, the current I_i going through each of these electrodes, as well as the anode potential ϕ_a, are recorded throughout the shot. For practical reasons, the voltages are measured right next to the voltage divider illustrated in figure 1(*b*), which is positioned some metres away from the electrodes, outside the chamber. Due to the finite resistance of these long connectors, the actual electrode potential ϕ_i thus has to be corrected given the current I_i and the resistance R_{w_i} of each of these connectors. These resistors were measured before the campaign with the multidisk electrode outside the chamber, with $R_{w_i} = 0.160$, 0.157, 0.167, 0.162 and 0.148 Ω for $i \in [\![1, 5]\!]$.

3. Baseline parameters

3.1. *Baseline profiles*

With our goal to highlight the effect of biasing on plasma parameters – particularly on the plasma potential – we briefly discuss the plasma parameter profiles measured for the selected operating point, first with the multidisk electrode pulled out of the chamber and then with the multidisk electrode in the machine but disconnected. This dataset is shown in figure 4. Starting with density (figure 4*e*,*f*), we measure a maximum of approximately 6×10^{18} m^{-3} in the centre during the main discharge, and a decrease with time after the discharge has been turned off ($t = 15$ ms). Both in the main discharge and in the afterglow, the density drops rapidly for $r \geq 25$ cm. This is consistent with a plasma column radius equal to the cathode radius. Indeed, the cathode radius is $r_c = 19$ cm, which considering flux conservation and the magnetic field ratio $\rho_B \doteq B_s/B_0 = 2$ between the source and the main chamber gives a plasma column radius $r_c\sqrt{\rho_B} \sim 27$ cm. The density data also shows an asymmetry, with density for positive x larger than density for negative x. This asymmetry does not vanish when averaging over time and is also larger than the shot-to-shot deviation, as shown by the error bars. Although the origin of this asymmetry remains to be determined, it might be evidence for probe perturbation. Negative x indeed corresponds to the far side of the machine, for which the probe arm extends past the central point. This could lead to perturbations, in particular if the plasma is rotating.

Moving on to figure 4(*c*,*d*), the electron temperature deduced from I–V characteristics is approximately 8 eV in the core during the main discharge on port #20, and drops to approximately 4 eV at the same location after the discharge has been turned off. Closer to the electrodes on port #34, a similar radial profile is observed but with an overall axial drop of approximately 5 eV in the main discharge and 2 eV in the afterglow, leading to peak temperatures of, respectively, 4 and 2 eV.

Lastly, the plasma potential ϕ_p (figure 4*a*,*b*) is relatively flat across the plasma column. It is, respectively, positive and negative by a few volts on port #20 and on port #34. The axial voltage drop between these two ports is approximately 5 V in the main discharge and approximately 2 V in the afterglow. This axial variation is consistent with the voltage drop expected from the axial temperature variation highlighted just above. Indeed the electron momentum equation gives

$$en_e\frac{\partial\phi_p}{\partial z} - \frac{\partial(n_eT_e)}{\partial z} + en_e\eta_\parallel j_z = 0 \tag{3.1}$$

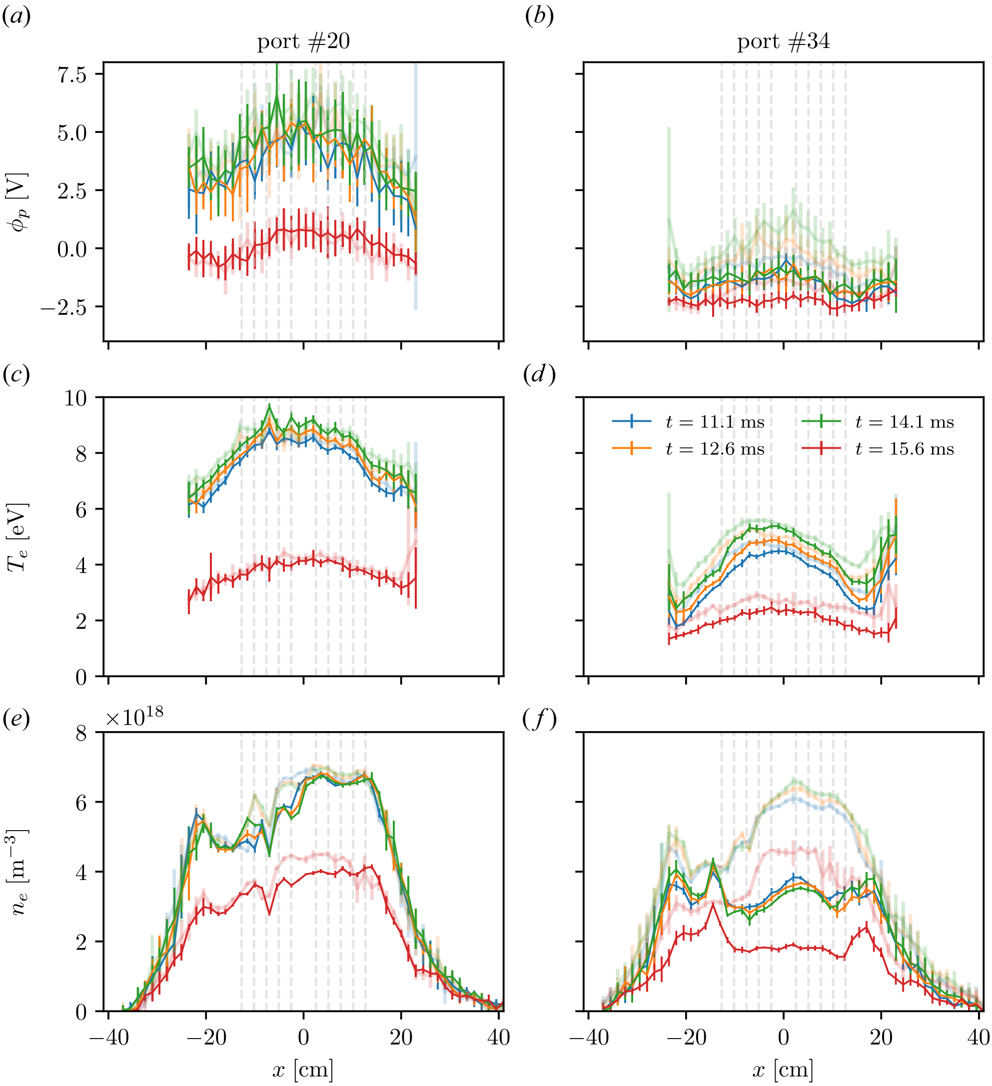

FIGURE 4. Radial profiles of the plasma potential (*a*,*b*) and the electron temperature (*c*,*d*) inferred from Langmuir probe sweeps, and of the floating potential (*a*,*b*, crosses) and of the density (*e*,*f*) deduced from floating probe and saturation current (without T_e corrections) at four times during the discharge, and on two ports: port #20 (*a*,*c*,*e*) and port #34 (*b*,*d*,*f*). The lighter curves correspond to the data taken with the electrodes outside the machine. The vertical dashed lines represent the electrode's position (when inserted).

so that neglecting axial current

$$\frac{\partial \phi_p}{\partial z} = \frac{1}{e}\frac{\partial T_e}{\partial z} + \frac{T_e}{e n_e}\frac{\partial n_e}{\partial z} > 0. \tag{3.2}$$

Over distances that are short compared with the axial density gradient length, which we verify in figure 4(*e*,*f*) correspond to the distance between port #20 and port #34, the first term on the right-hand side dominates. The axial voltage drop is then equal to lowest order to the axial temperature variation.

Parameter	Value
Gas	helium
Discharge current I_d (kA)	3.2
Main chamber magnetic field B_0 (T)	0.1
Magnetic field ratio ρ_b	2
Plasma density n_e (m^{-3})	5×10^{18}
Electron temperature T_e (eV)	5
Plasma radius (cm)	25
Plasma length (m)	11

TABLE 1. Typical machine and plasma parameters for the operating point targeted in this campaign.

Finally, we note that introducing the disconnected electrodes to the plasma produces a noticeable effect at port #34 which is located closest to the electrodes. A significant density depletion, consistent with enhanced losses, occurs in the central region where the field lines connect to the electrodes. A closer examination here also reveals a modest drop in T_e – and consequently ϕ_p.

3.2. *Currents*

From the plasma density n_e and electron temperature T_e measured above, we can deduce estimates for the ion saturation current density $j_{\mathrm{is}} \doteq e n_e c_s$ with $c_s \doteq \sqrt{k_B T_e / m_i}$ the ion sound speed. Using $n_e = 5 \times 10^{18}\ \mathrm{m}^{-3}$ and $T_e = 5$ eV (see table 1) as a baseline operating point in this campaign, we obtain a characteristic ion saturation current density

$$j_{\mathrm{is}}^{\diamond} = 8.7\ \mathrm{kA\ m}^{-2}. \tag{3.3}$$

For reasons that will become clear later, it is informative to compare this current to the current density deduced from the discharge current I_d. Considering a uniform emission on the cathode, and accounting for the anode transparency $\iota = 0.66$ (Qian *et al.* 2023), the current density of primary electrons injected in the plasma through the anode during the main discharge is

$$j_{\mathrm{inj}} = -\frac{\iota I_d}{\pi \rho_B r_c^2}, \tag{3.4}$$

where ρ_B is the field ratio previously defined. For the discharge current $I_d \sim 3.2$ kA shown in figure 3 and $\rho_B = 2$ one gets $j_{\mathrm{inj}} = -9.3\ \mathrm{kA\ m}^{-2}$.

Although the amplitude of these currents will vary with the location through the spatial dependence of T_e and n_e on one hand, and with the exact discharge current on the other hand, the important point here is to note that in the conditions investigated here these two terms are of comparable magnitude.

4. Effect of biasing on the radial profile of plasma parameters

4.1. *Biasing profiles*

We choose six biasing profiles to impose on the multidisk electrode to study the effect of differential electrode biasing on plasma parameters. Our motivation for choosing these six specific biasing scenarios, which are listed in table 2 and illustrated in figure 5, is that they cover different polarities with respect to machine ground as well as different directions of

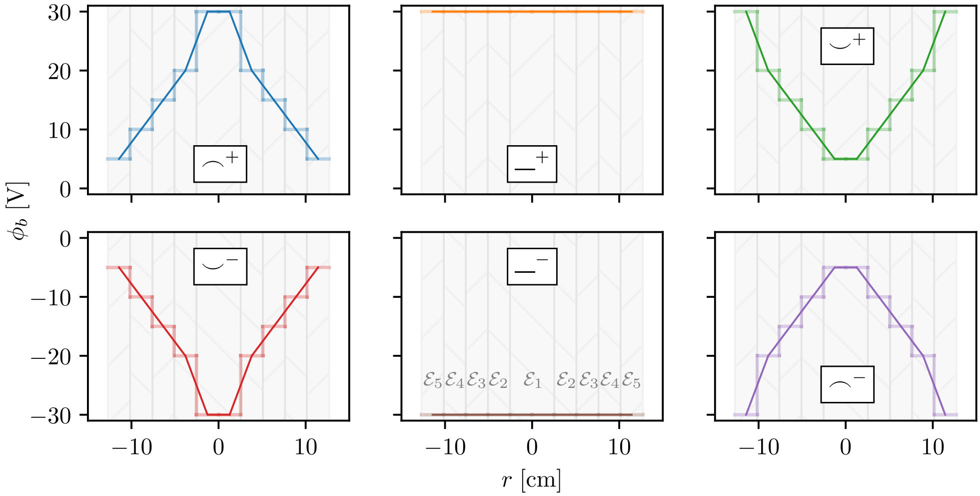

FIGURE 5. Potential profile imposed on the electrodes for the six biasing scenarios tested in this campaign, as listed in table 2. The thin solid-coloured lines represent the continuous targeted profile, while the thicker coloured segments represent the actual step-like profile imposed on the electrodes. The grey hatched regions represent the position of the different electrodes $\mathcal{E}_i$.

Biasing profile	Shorthand	Color code
Positive, concave-down (negative gradient)	$\frown^+$	🟦
Positive, flat	$\_^+$	🟧
Positive, concave-up (positive gradient)	$\smile^+$	🟩
Negative, concave-up (positive gradient)	$\smile^-$	🟥
Negative, flat	$\_^-$	🟫
Negative, concave-down (negative gradient)	$\frown^-$	🟪

TABLE 2. Six biasing scenarios studied in this campaign. The amplitude is 30 V in all cases.

the radial gradient of the potential. In other words, we examine the effect of both positive and negative biases, as well as concave-up and -down potential profiles. The amplitude in all cases is 30 V, though as mentioned above the resistance of the connectors is such that the actual bias on the electrode can be slightly larger or smaller depending on the current drawn by this particular electrode.

A consequence of this resistance, and of the biasing circuit shown in figure 1(*b*), is that the plasma potential profiles already show a weak dependence on the particular biasing scenario implemented before the active biasing phase. This is illustrated in figure 6, which corresponds to $t = 11.1$ ms, that is 0.9 ms before the biasing power supply is turned on. Indeed, even if the bias is off, electrodes are not floating. They are connected through the connectors and the voltage divider. Because the position of a given pin on the voltage divider differs with the different biasing scenarios, the resistance between a given electrode and ground also differs. This leads to a different electrode bias, and from there to a different plasma potential in front of this electrode. Note that the larger error bars seen

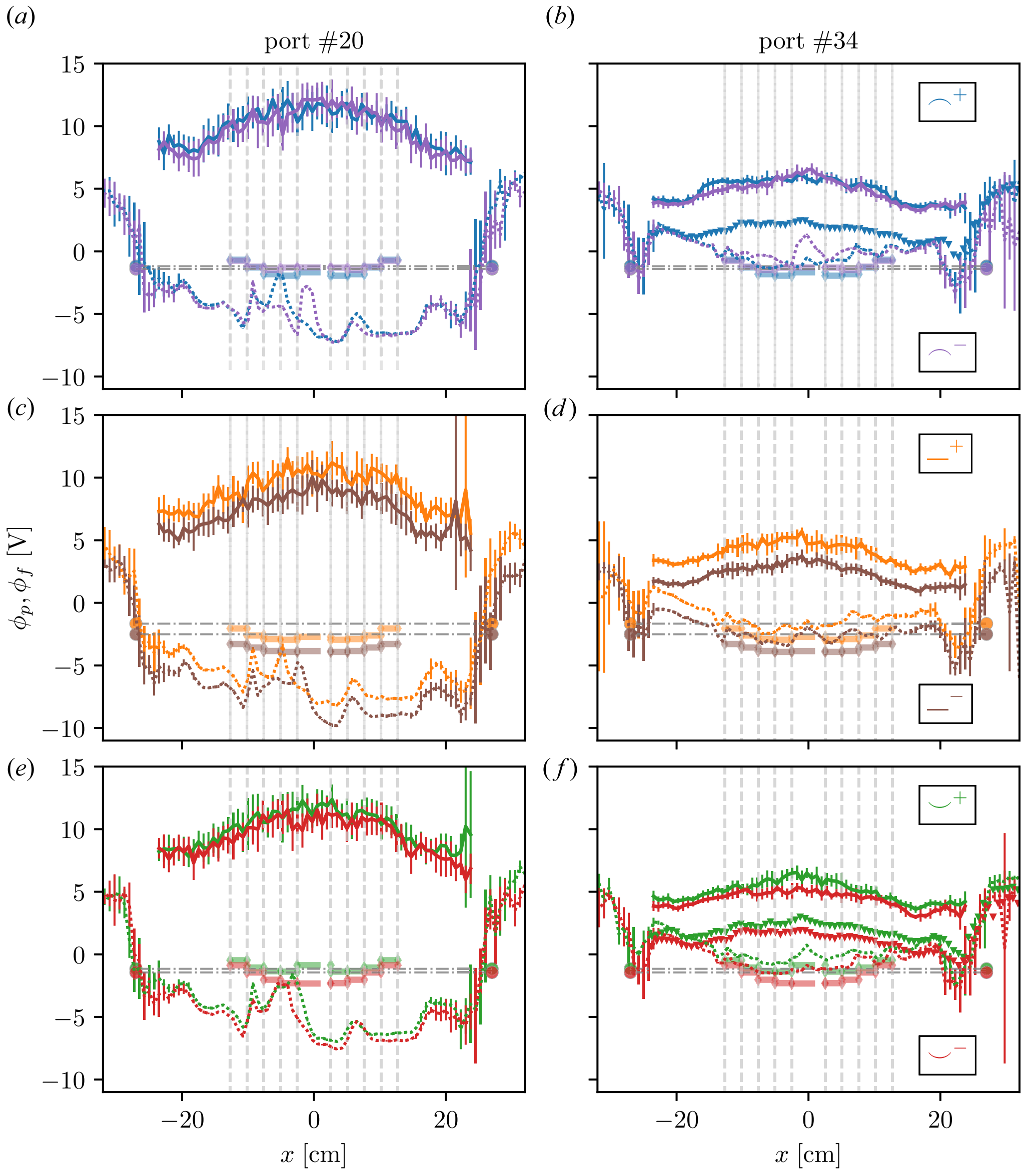

FIGURE 6. Plasma (solid line) and floating (dotted line) potential profiles on two ports (#20 (*a*,*c*,*e*), #34 (*b*,*d*,*f*)) at $t = 11.1$ ms (before biasing) for the six biasing scenarios listed in table 2. The vertical dashed lines represent the electrodes position. The thicker and lighter coloured horizontal lines represent the electrodes potential ϕ_i at that time. The horizontal grey dashed lines with coloured circles symbols represent the anode potential ϕ_a. The ▼ symbols in (*b*,*d*,*f*) correspond to plasma potential inferred from the emissive probe on port #33 (when available).

in figure 6 for $r \gtrsim 25$ cm corresponds to the region beyond the projected cathode radius $r_c\sqrt{\rho_B} \sim 27$ cm where the density drops rapidly.

We also verify in figure 6 that, while there is a small offset of approximately 2 V between the two datasets, the plasma potential estimated from $I(V)$ sweeps on port #34 (solid lines) is consistent with that obtained approximately 60 cm away from the emissive probe on port #32 (triangle symbols). The radial dependence predicted by both methods is notably remarkably similar. This is particularly noteworthy in that these two datasets were obtained in different runs (days apart), so that small variations in plasma parameters cannot be excluded.

4.2. *Potential profiles under active biasing*

As shown in figure 7, biasing has a very noticeable effect on the radial profile of plasma potential during the main discharge ($t = 12.6$ ms). We can make a number of general observations before attempting to explain this plasma response in the next section.

First, the amplitude of the plasma potential variations in response to biasing is significant. For the conditions used here, one finds $-15 \leq \phi_p \leq 35$ V with active biasing, compared with $5 \leq \phi_p \leq 10$ V with biasing off. The amplitude of this shift is thus comparable to the maximum bias of ±30 V applied on the electrodes. This suggests that only a modest fraction of the applied bias is lost through the sheaths (Poulos 2019; Trotabas & Gueroult 2022). Second, the radial profile of the plasma potential is found to track – if not to be driven by – the applied bias profile. More precisely, figure 7 shows that it is the floating potential $\phi_f(r, z_{34})$ rather than the plasma potential $\phi_p(r, z_{34})$ which tracks the applied bias $\phi_b(r)$, and that concave-down profiles which have negative radial gradients (blue and purple) appear to be more easily passed into the plasma column than those with positive gradients (red and green). Lastly, we note that these variations in plasma potential are accompanied by smaller yet significant variations in anode potential ϕ_a. The anode potential is indeed observed to vary in these conditions from -11 to 11 V depending on the biasing scenario.

Looking more closely at the ordering between the plasma potential and the electrode bias, we find that for constant applied bias across the electrodes (orange and brown) the plasma potential is larger than the bias on any electrode. The difference between the plasma potential on port #34 and the applied bias on the electrodes is then relatively uniform radially. For non-uniform biasing profiles, the overall profile appears to be set by the condition that the plasma potential is to be slightly more positive than the most positive electrode in the region in front of this electrode. Because the plasma potential does not precisely follow the applied bias, the voltage drop between a given electrode $\mathcal{E}_i$ and the plasma potential in front of it varies with each electrode. Anticipating our discussion in the next section, we see that this will lead to non-uniform currents to the electrodes.

Irrespective of the biasing case, the plasma potential profiles measured on ports #20 and #34 have almost the same shape, at least in the region in front of the electrodes. In fact one verifies that they can be simply deduced from one another via a uniform shift up (going from port #34 to port #20) or down (going from port #20 to port #34). As mentioned above, this shift is consistent with a radially uniform temperature drop between the two axial locations. Other than for this temperature effect, the data in figure 7 shows that the imprint of the bias on the plasma potential profile is recovered at least 6 m away from the multidisk electrodes.

Finally, we verify in figure 8 that the strong influence of the biased electrodes on the plasma potential, as well as the general trends identified above, persist in the afterglow after the main discharge is shut off. In the afterglow, however, we find that the plasma potential profile is much closer to the floating potential profile. This behaviour is consistent with the rapid drop in T_e observed in the afterglow.

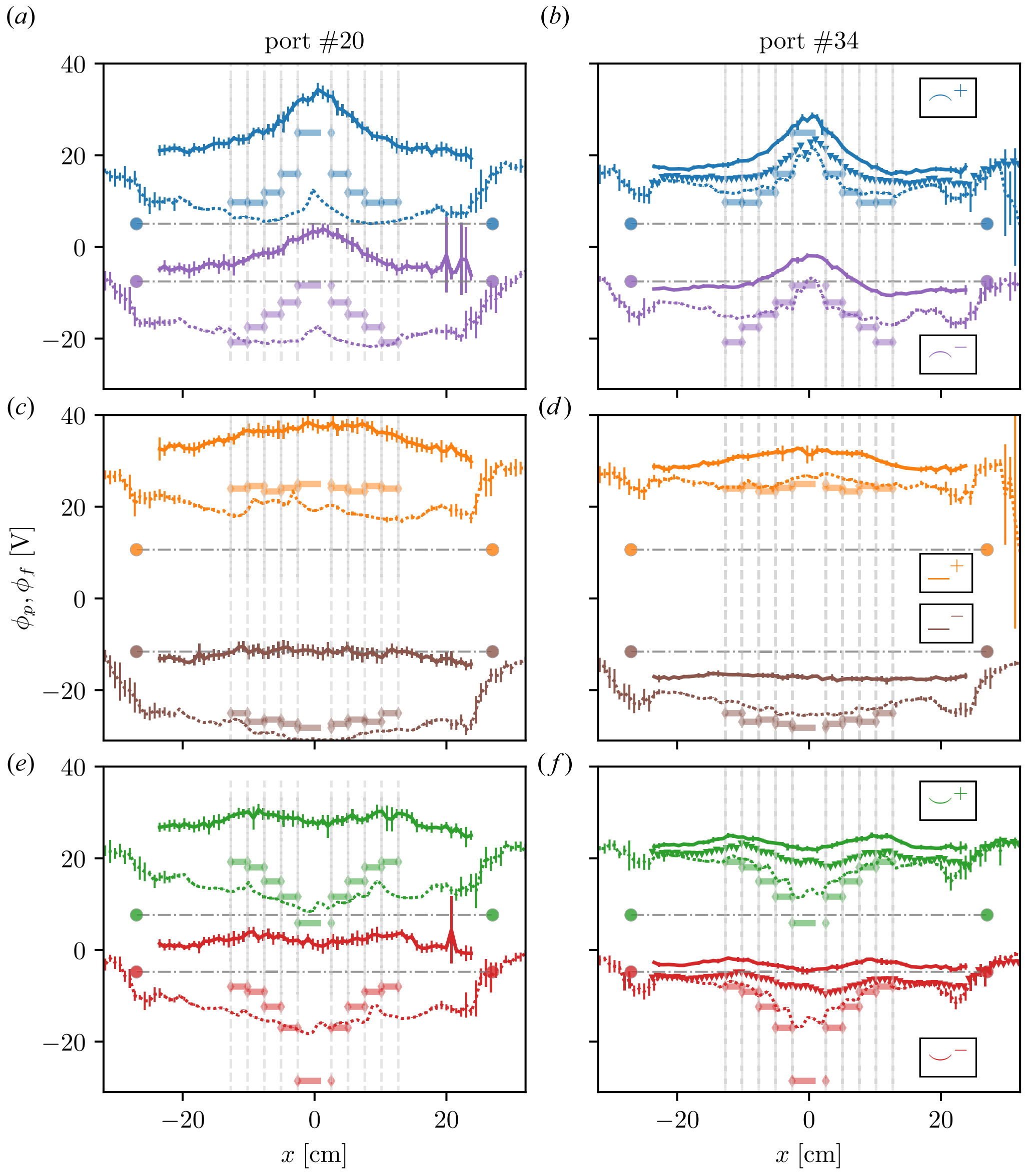

FIGURE 7. Plasma (solid line) and floating (dotted line) potential profiles on two ports (#20 (a,c,e), #34 (b,d,f)) at $t = 12.6$ ms (i.e. in the main discharge during biasing) for the six biasing scenarios listed in table 2. The vertical dashed lines represent the electrodes position. The thicker and lighter coloured horizontal lines represent the electrodes potential ϕ_i at that time. The horizontal grey dashed lines with coloured circles symbols represent the anode potential ϕ_a. The ▼ symbols in (b,d,f) correspond to plasma potential inferred from the emissive probe on port #33 (when available).

4.3. *Density and temperature profiles under active biasing*

Looking now at the effect of biasing on other plasma parameters, figure 9 plots the radial profiles of plasma density n_e and of electron temperature T_e during active biasing in the main discharge ($t = 12.6$ ms), just in front of the electrodes (port #34).

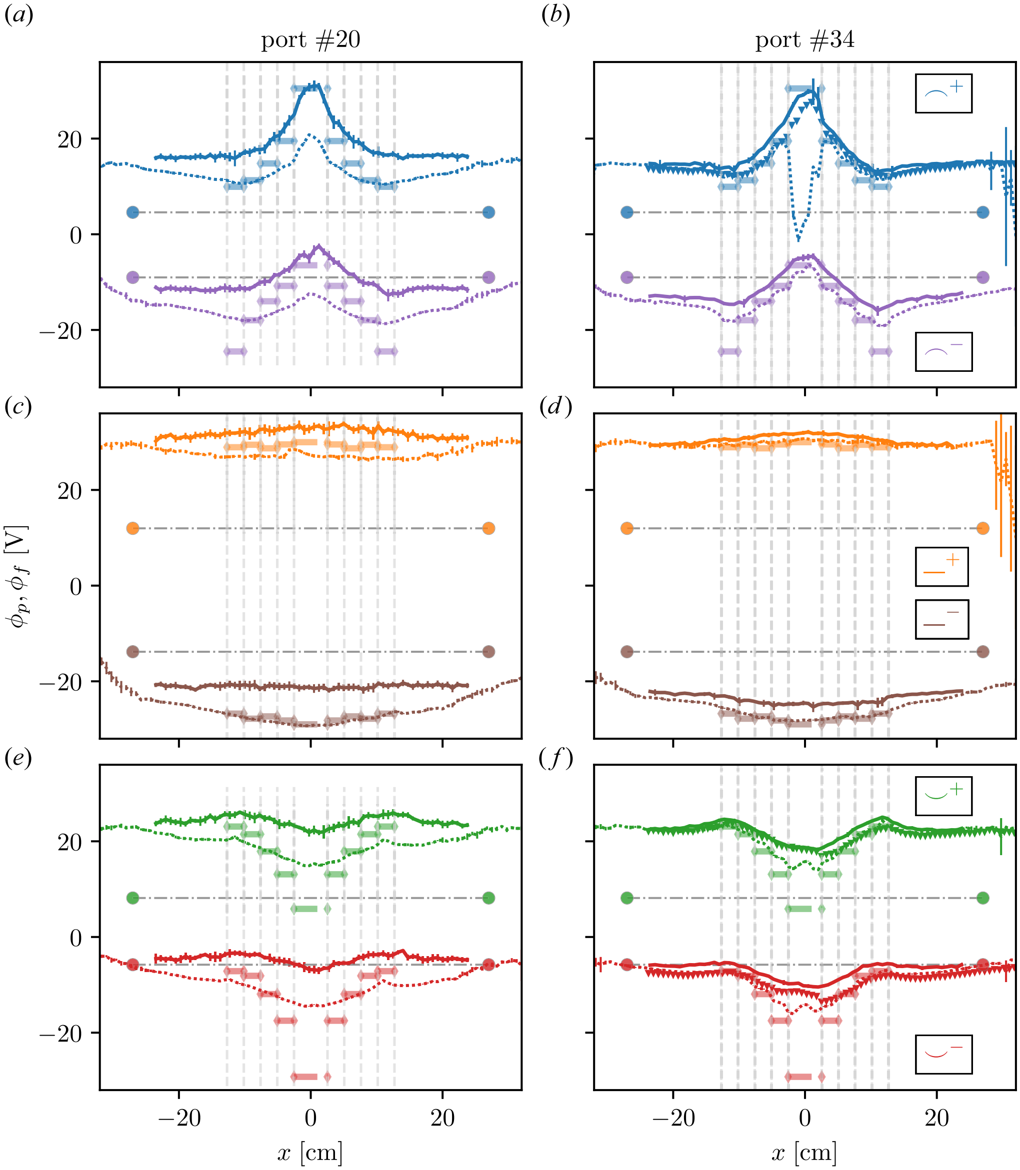

FIGURE 8. Plasma (solid line) and floating (dotted line) potential profiles on two ports (#20 (*a*,*c*,*e*), #34 (*b*,*d*,*f*)) at $t = 12.6$, $t = 15.6$ ms (i.e. in the afterglow during biasing) for the six biasing scenarios listed in table 2. The vertical dashed lines represent the electrodes position. The thicker and lighter coloured horizontal lines represent the electrodes potential ϕ_i at that time. The horizontal grey dashed lines with coloured circles symbols represent the anode potential ϕ_a. The ▼ symbols in (*b*,*d*,*f*) correspond to plasma potential inferred from the emissive probe on port #33 (when available).

Starting with the density, one observes for non-uniform biasing scenarios a decrease in density in the region in front of the most positive electrode. This behaviour is most noticeable for the negative gradient biasing scenarios ($\frown^-$, figure 9*f*, and $\frown^+$, figure 9*a*), for which a clear density drop of 30 %–50 % is observed in front of the central electrode

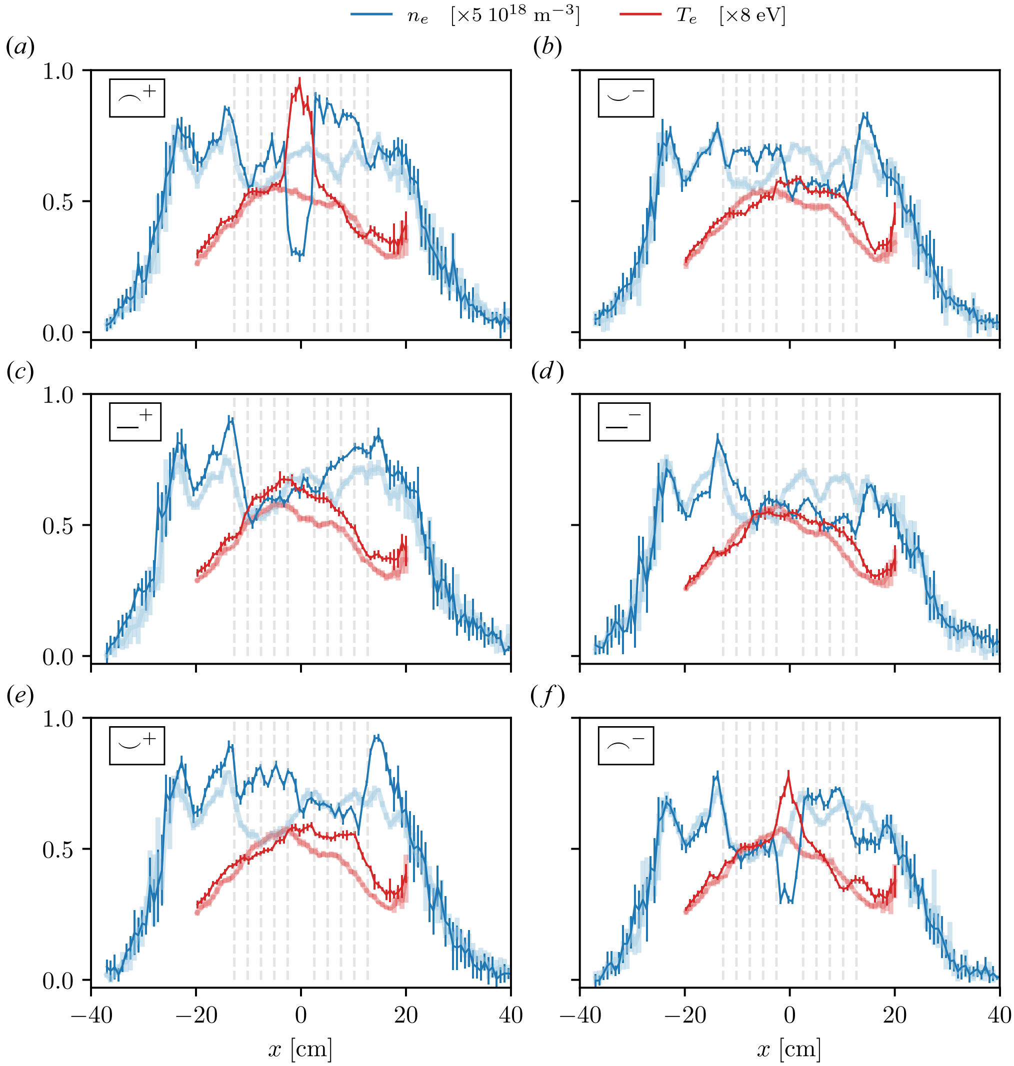

FIGURE 9. Density (blue) and temperature (red) radial profiles on port #34 before active biasing ($t = 11.1$ ms, thicker lighter colour lines) and during active biasing in the main discharge ($t = 12.6$ ms, thinner solid lines) for the six biasing scenarios listed in table 2 (six different panels). The vertical dashed lines represent the electrodes position. Density and temperature are normalised to 5×10^{18} m^{-3} and 8 eV, respectively.

$\mathcal{E}_1$. Trying to make sense of this density profile hollowness, we see in figure 7 that the electrode with the highest potential is also the region where the sheath is the smallest. As a result, this is where the largest electron current density is drawn at the electrode. As we will show, this electron current density can become comparable to the current density j_{inj} injected from the cathode, in which case one expects a decrease in plasma density in this region as a result of depletion, consistent with observations. It is also worth noting that the hollowness observed here share traits with what is referred to as plasma hole structures (Nagaoka *et al.* 2002; Tanaka 2019), though there are a number of differences suggesting they may have different origins. An important one is that peak rotation is found to occur at the edge of the hollow region in plasma holes, whereas as we will show in § 6 it appears to be well within the depletion region in the experimental data reported here.

Looking more closely, the decrease in density in front of the most positive electrode appears to be accompanied by a density increase in the adjacent region. This is notably visible for $x > 0$ and the positive gradient scenarios ($\smile^{-}$, figure 9*b*, and $\smile^{+}$, figure 9*e*), for which the density appears to drop when actively biasing for $r \leq 12.5$ cm, but to rise for $r > 12.5$ cm (i.e. past the outer edge of the outermost electrode $\mathcal{E}_5$). The reason for this behaviour, if confirmed, remains to be determined. It may be related to the fact that, as discussed later in § 5.3, that the current to the anode must remain globally balanced during the main discharge.

In this same figure we see that this local depletion is accompanied by an increase in the local electron temperature T_e. This is particularly clear for the negative gradient biasing scenarios ($\frown^{-}$, figure 9*f*, and $\frown^{+}$, figure 9*a*), for which a significant increase in T_e is seen in front of the central electrode $\mathcal{E}_1$. We note that since the density is here deduced directly from I_{sat}, and thus does not account for the effect of a change in T_e through the ion sound speed, this local heating will lead to an even stronger density drop. Exploring how these effects vary axially, that is with the distance from the multidisk electrode, we found (not shown here) that both the depletion and heating were clearly recovered in the density and temperature profiles measured on port #20, that is approximately 6 m away from the electrodes. Finally, these features are observed to persist in the afterglow. In fact the depletion is even more pronounced in the afterglow, with the plasma density then approaching zero. This is because there is in this case no longer an electron beam to act as a plasma source to replenish the depleted flux tube.

5. Model for the plasma potential response to biasing

Having highlighted in the previous section how different biasing profiles imposed on the multidisk electrode lead to different plasma potential profiles and anode potential, we now try to shed light on the dynamics at play. We begin by discussing how the different plasma potential profiles observed for the different biasing scenarios can be understood in terms of the axial current drawn at the electrodes. We then show how the current balance at the anode forces the anode potential to respond to the plasma potential created by the multidisk electrodes. Throughout this section, we assume that the plasma column is axisymmetric with radial profiles consistent with the profiles along x presented in the previous section.

5.1. *Voltage drop along field lines*

The first element in analysing the evolution of the plasma potential with biasing is to appreciate that although it is small, the non-zero axial plasma resistivity can be the source of significant (with respect to the applied bias) axial voltage drops.

To see this, recall that, for the low operating pressure used on LAPD, the dominant contribution to parallel resistivity is electron–ion collisions (Poulos 2019). The parallel resistivity is thus the parallel Spitzer resistivity,

$$\eta_{ei} = 1/\sigma_{\parallel}^{ei} = \frac{1}{1.96}\frac{m_e \nu_{ei}}{n_e e^2} \tag{5.1}$$

with

$$\nu_{ei} = \frac{n_e Z^2 e^4 \varLambda_c}{6\sqrt{2}\pi^{3/2}\epsilon_0^2\sqrt{m_e}(k_B T_e)^{3/2}} \tag{5.2}$$

the Coulomb collision frequency and $\varLambda_c$ the Coulomb logarithm. For the typical plasma parameters given in table 1 one gets $\eta_{ei} \sim 7 \times 10^{-5}\ \Omega$ m. From there one finds that the

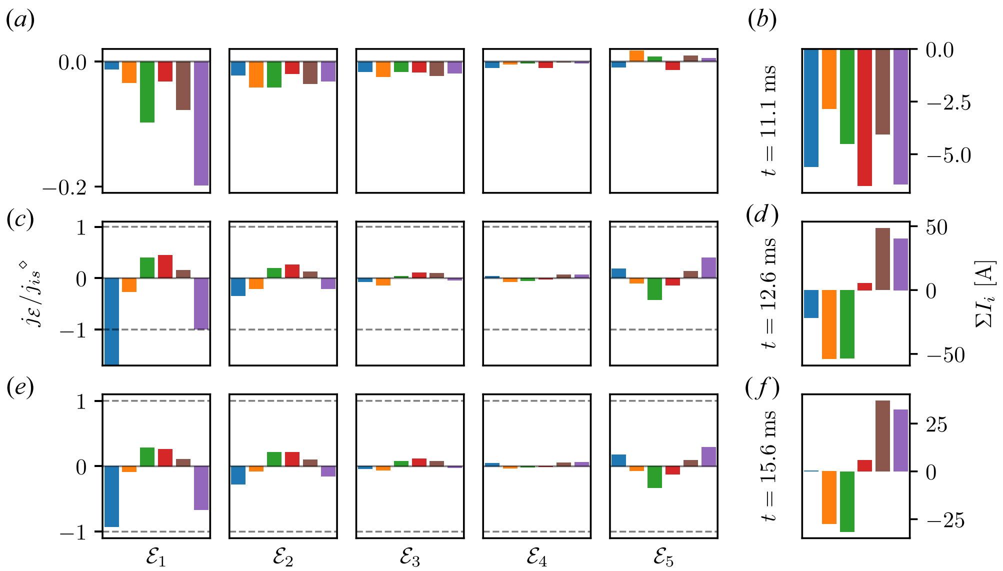

FIGURE 10. Current density $j_\mathcal{E}$ on each electrode $\mathcal{E}_i$ for $i \in [\![1, 5]\!]$ (*a*) and total current ΣI_i drawn by the multidisk electrode (*b*) at the three different instants of interest (rows) and for all biasing cases (colour code) shown in table 2. The current density is here normalised by the characteristic current density ${j_{\mathrm{is}}}^\diamond$ (see (3.3)), and obtained by assuming a uniform current distribution on each electrode. The horizontal dashed grey lines highlights $j_\mathcal{E} = \pm {j_{\mathrm{is}}}^\diamond$.

voltage drop along field lines over a distance s for a given parallel current $j_\parallel$ is

$$\varDelta_\parallel \phi_p(r) = \int_0^s \eta_{ei} j_\parallel(r, z)\,\mathrm{d}z. \tag{5.3}$$

Using as an estimate the characteristic ion saturation current density $j_{\mathrm{is}}^\diamond = 8.7$ kA m^{-2} defined in (3.3) this leads to $\eta_{ei} j_{\mathrm{is}} \sim 0.6$ V m^{-1}. Integrating over the 11 m separating the anode from the multidisk electrode, this would lead to $\varDelta_\parallel \phi_p \sim 7$ V, which is indeed significant compared with the ±30 V of applied bias.

5.2. *Current driven plasma potential radial profile*

To confirm this finding and the importance of a voltage drop along field lines in the quasineutral plasma, one still needs to know how large the actual parallel current $j_\parallel$ is compared with the characteristic ion saturation current density $j_{\mathrm{is}}^\diamond$. To do so, we assume current conservation along magnetic field lines to use here as a proxy the current density, $j_{\mathcal{E}_i}$ which is deduced from the current $I_i = j_{\mathcal{E}_i} \mathcal{A}_i$ collected on each electrode $\mathcal{E}_i$ of surface $\mathcal{A}_i$. This dataset is shown in figure 10. Beyond a substantial overall increase in current drawn when bias is turned on, one verifies that current densities $|j_{\mathcal{E}_i}|$ exceeding $j_{\mathrm{is}}^\diamond$ are collected on the innermost electrode $\mathcal{E}_1$ when this electrode is the most positive (negative potential gradients on the electrodes, blue and purple). This confirms that the axial currents that result from active biasing are indeed the source of voltage drops along field lines of more than 10 V. Also, recalling from § 3.2 that the injected current density j_{inj} is comparable in absolute value to the ion saturation current density $j_{\mathrm{is}}^\diamond$, the observation in figure 10 that $|j_{\mathcal{E}_1}|$ is comparable to $j_{\mathrm{is}}^\diamond$ for the two negative-gradient biasing scenarios further supports the idea of a depletion driven by the biased electrode.

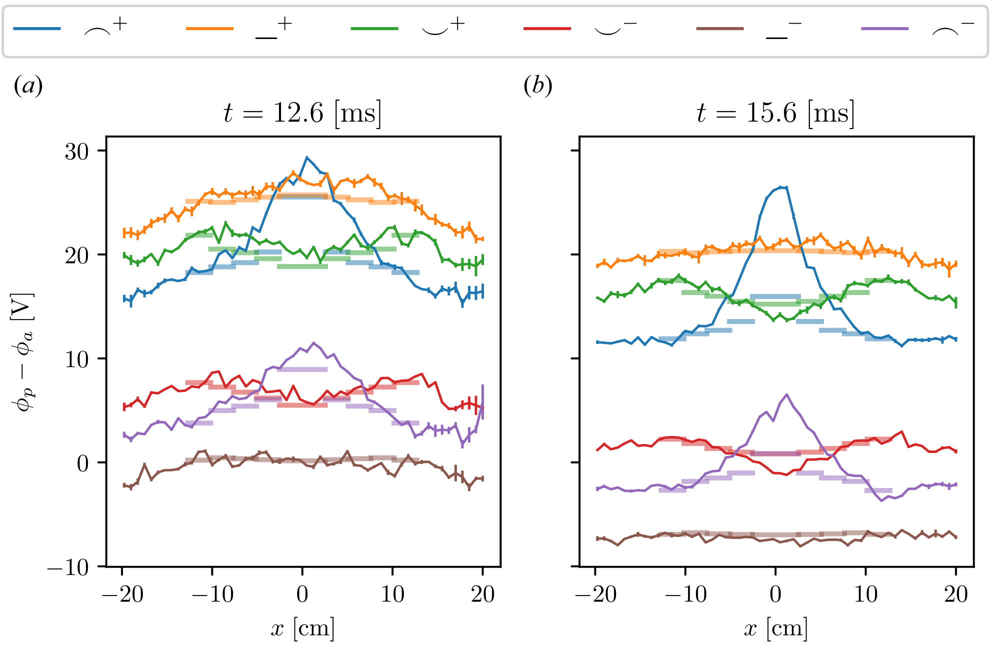

FIGURE 11. Radial profile of the plasma potential $\phi_p(r, z_{20})$ minus the anode potential ϕ_a measured at $t = 12.6$ (*a*) (main discharge) and $t = 15.6$ ms (*b*) (afterglow) on port #20 (solid lines with error bars) compared with the profiles constructed from an offset φ and the voltage $\eta_{ei} j_{\mathcal{E}_i} l$ (thick lines, see (5.4)), with $j_{\mathcal{E}_i}$ the current density measured on electrode $\mathcal{E}_i$ at this instant, $l = z_a - z_{20} = 6$ m for the distance between the anode and port #20, and $\eta_{ei} = 7 \times 10^{-5}\ \Omega$ m which corresponds to the baseline parameters given in table 1.

Exploring this idea further, we can examine how the radial dependence of $j_{\mathcal{E}}$ can possibly explain the observed radial profile of the plasma potential $\phi_p(r)$. To do so, we simply construct the radially dependent axial voltage drop $\varDelta_{\parallel}\phi_p(r)$ computed from a constant and uniform resistivity η_{ei} and the time-dependent and electrode dependent $j_{\mathcal{E}_i}$. Comparing these simple results with the actual plasma potential profiles $\phi_p(r)$ as done in figure 11, we see that this simple model reproduces very well the radial variations of the plasma potential. Specifically, figure 11 shows that

$$\phi_p(r, z_{20}) \approx \phi_a + \varphi + \eta_{ei} j_{\mathcal{E}_i}(z_a - z_{20}), \tag{5.4}$$

where φ is an offset and ϕ_a is the anode potential. Although, as summarised in table 3, the parameters ϕ_a and φ are both biasing scenario dependent, they are importantly radially uniform. The fit observed in figure 11 thus supports further the idea that the plasma potential profile is driven by the axial currents $j_{\mathcal{E}_i}$ collected on biased electrodes. This fit is made more remarkable by the fact that we chose here for simplicity to use a constant value $\eta_{ei} = 7 \times 10^{-5}\ \Omega$ m, and thus did not capture the radial, temporal and biasing scenario dependencies of η_{ei} expected from the radial, temporal and biasing scenario dependencies of T_e. One for instance expects from (5.1) and (5.2) the resistivity to increase as T_e decreases going from the main discharge to the afterglow, which would imply that the voltage drops in the afterglow are actually larger than predicted. The non-captured drop in T_e could thus explain the observation that the fit in figure 11 is better in the main discharge than in the afterglow.

Biasing scenario		Offset φ [V]		Anode potential ϕ_a [V]	
		12.5 ms	15.5 ms	12.5 ms	15.5 ms
$\frown^+$	🟦	18	12	5	4
$\_^+$	🟧	25	20	11	12
$\smile^+$	🟩	22	17	8	8
$\smile^-$	🟥	8	2	-5	-6
$\_^-$	🟫	0	-7	-11	-14
$\frown^-$	🟪	4	-3	-8	-9

TABLE 3. Offset φ to be added to the anode potential ϕ_a and the axial voltage drop $\eta_{ei} j_\parallel l$ to reproduce the observed radial plasma potential profile $\phi_p(r, -l)$ on port #20. For comparison $\varphi = 11 \pm 1$ V for all scenarios at $t = 11.6$ ms, that is prior to active biasing.

Summing up our observations, radial potential shaping in the plasma is achieved by drawing different axial currents on the different electrodes. On the other hand the reason for the offset φ in (5.4) remains at this point unclear. To answer this question, we need to look at the anode–cathode system and how its dynamics is coupled to that of the plasma, as we will do next.

5.3. *Current balance at the anode*

We now would like to explain the offset φ needed to reproduce the plasma potential in (5.4), and because this offset is added to the anode potential ϕ_a we must also consider the anode dynamics.

A key element to understanding the response of the anode–plasma system to biasing is the overall current balance in the machine. During the main discharge, an electron current ιI_d, with ι the anode transparency, is injected through the mesh anode into the main chamber. This is equivalent to the current density j_{inj} defined in (3.4). Although the anode–cathode system is floating with respect to the machine ground (Qian *et al.* 2023), this injected current $-\iota I_d$ must be balanced by an equal excess of electron current returning to the anode from the plasma in the main chamber. This in turn sets constraints on the voltage drop one can have between the anode potential ϕ_a and the plasma potential in front of the anode $\phi_p(r, z_a)$. Indeed, assuming an ion sheath, the current density collected on the anode is (Poulos 2019; Trotabas & Gueroult 2022)

$$j_a(r) = j_{\text{is}} \left(1 - \exp\left[\Lambda + \frac{\phi_a - \phi_p(r, z_a)}{T_e}\right]\right) \tag{5.5}$$

with

$$\Lambda = \ln\left[\sqrt{\frac{m_i}{2\pi m_e}}\right] \tag{5.6}$$

a parameter that is approximately 3.5 in helium. The anode potential ϕ_a and the plasma potential in front of the anode $\phi_p(r, z_a)$ must thus adjust so that overall

$$j_{\text{inj}} \pi \rho_B r_c^2 = \int_0^{\sqrt{\rho_b} r_c} 2\pi r \, \mathrm{d}r j_a(r). \tag{5.7}$$

Note importantly that this condition is global as opposed to local, so that there can still be current along magnetic field lines, i.e. $j_a(r) \neq j_{\text{inj}}$.

We now see the origin of the offset φ in (5.4). It is the height of the anode sheath required to ensure the needed electron return current $-\iota I_d$ to the anode.

5.4. *Effect of biasing on the anode sheath height*

To see why the anode sheath and thus the offset φ depend on the biasing scenario, we need to consider the total current balance.

In the absence of parallel current, we can safely disregard the dynamics at the multidisk electrode and focus exclusively on the anode. Assuming further a uniform plasma potential in front of the anode, $j_a = j_{\mathrm{inj}}$ and (5.5) then gives

$$\varphi \approx \left[\Lambda - \log\left(1 - \frac{j_{\mathrm{inj}}}{j_{\mathrm{is}}}\right)\right] T_e, \tag{5.8}$$

where we recall from (3.4) that $j_{\mathrm{inj}} < 0$. For comparable current densities j_{inj} and $j_{\mathrm{is}}^{\diamond}$ this would lead to a voltage drop of 2.5–$3T_e$.

This regime of negligible parallel current happens to be relatively representative of the regime before active biasing ($t \leq 12$ ms). As shown in figure 10(*a*), the current density on the electrodes is indeed much smaller than to the ion saturation current density $j_{\mathrm{is}}^{\diamond}$. From (5.3) this implies a negligible voltage drop along field lines, so that we can in first approximation consider $\phi_p(r, z_a) \approx \phi_p(r, z_{20})$. Now, looking back at figure 6(*a*,*c*,*e*), we find that the plasma potential on port #20 is approximately 10 to 15 V higher than the anode potential ϕ_a. This voltage drop is relatively consistent with the 2.5–$3T_e$ predicted above, given the temperature $6 \leq T_e \leq 8$ eV measured on port #20. It is also very consistent with the offset $\varphi = 11 \pm 1$ V computed at this instant for all biasing scenarios, supporting the interpretation of φ in terms of the anode sheath height.

In contrast, we have seen in figure 10(*c*,*e*) that current densities comparable or even larger in amplitude than $j_{\mathrm{is}}^{\diamond}$ are collected on the multidisk electrode during active biasing. Beyond leading, as discussed earlier, to a significant axial voltage drop along the field line in the plasma, this collected current also modifies the total current balance. A negative current drawn on the multidisk electrode must be compensated by a decrease in the electron current collected at the anode, which is achieved by increasing the sheath height. Going back to table 3 and figure 10(*d*), we verify that the offset indeed is larger for positive biases (blue, orange and green), and that the larger the amplitude of the total current drawn $\Sigma I_i < 0$, the larger the offset. Conversely, a positive current drawn on the multidisk electrode, which for an ion sheath implies a reduced electron current, must be compensated by an increase of the electron current collected at the anode, which is achieved by decreasing the sheath height. Going once again back to table 3 and figure 10(*d*), we verify this time that the offset is indeed smaller for negative biases (red, brown and purple), and that the larger the amplitude of the total current drawn $\Sigma I_i > 0$, the smaller the offset. Finally, the offset φ prebiasing, for which the potential ϕ_i on the electrodes is as shown in figure 6 only a few volts below ground, seats as expected in between those of positive and those of negative biases.

Finally, we note in table 3 that the offset changes, and more precisely decreases slightly, when moving into the afterglow. This behaviour was to be expected as there is in this case no longer current injection at the anode, and thus no longer the need to collect this current back to the anode from the plasma.

5.5. *Discussion*

In summary, the analysis proposed here of the experimental results obtained in this campaign indicate that the plasma potential profile is primarily controlled via the boundary condition imposed on a given field line by the multidisk electrode. This suggests that the dynamics is essentially axial (i.e. parallel to the background magnetic field), which is consistent with earlier results on LAPD by Jin *et al.* (2019), and with the analysis of these results proposed by Poulos (2019) in the limit that $\tau \ll 1$ (see (1.1)). This also suggests that more pronounced profiles, e.g. stronger radial electric field, could be produced by drawing appropriate currents on the biased end-electrodes.

A few comments are, however, called for at this point. Jin *et al.* (2019) used hot electrodes producing parallel current densities a few times the ion saturation current density (in amplitude), which is significantly larger than those measured for cold electrodes in this study. This weaker current could have suggested a larger voltage drop across the sheath (Poulos 2019; Trotabas & Gueroult 2022), contrary to what was observed in the results reported here. The reason for this finding is twofold. First, in biasing with respect to the chamber wall as opposed to the anode, the anode was here free to self-adjust, limiting in turn the amplitude of the voltage drop across the sheath formed in front of the multidisk electrode for negative biases. Second, although they remain smaller than those produced by hot electrodes, the parallel currents generated here for positive biases were large enough to support axial voltage drops along field lines that are comparable to the applied bias, limiting again the voltage drop across the sheath.

Another noteworthy difference is that, by collecting large electron currents, the positive biases that lead here to noticeable radial potential profiles concurrently lead to depletion on the magnetic field lines connected to the most positive electrodes. This is in contrast with hot negatively biased electrodes as used by Jin *et al.* (2019), for which a density increase was observed.

6. Biasing driven plasma rotation

Having established in the previous sections that differentially biasing the multidisk electrodes with respect to the machine ground has a clear effect on the radial profile of plasma potential $\phi_p(r)$ in the machine, we can now infer how these different equilibria lead to different rotation profiles.

6.1. *Cross-field rotation from end-electrodes biasing*

In a linear machine with $\boldsymbol{B} = B_0\hat{\boldsymbol{e}}_z$ radial gradients of pressure $p(r)$ and plasma potential $\phi_p(r)$ are the source of different azimuthal drifts that can both contribute to plasma rotation. One is the diamagnetic drift $\boldsymbol{\varOmega}_D = \varOmega_D\hat{\boldsymbol{e}}_z$ where

$$\varOmega_D = -\frac{|\nabla p \times \boldsymbol{B_0}|}{rqnB_0^2} = \frac{1}{rqnB_0}\frac{\partial p(r)}{\partial r} \tag{6.1}$$

with q the signed particle charge. The other is the $\boldsymbol{E} \times \boldsymbol{B}$ drift, which leads to a cross-field angular plasma frequency $\boldsymbol{\varOmega}_{E\times B} = \varOmega_{E\times B}\hat{\boldsymbol{e}}_z$ with

$$\varOmega_{E\times B} = \frac{1}{rB_0}\frac{\partial \phi_p(r)}{\partial r}. \tag{6.2}$$

A positive potential radial gradient thus leads to $\varOmega_{E\times B} > 0$ and a cross-field drift in the direction of the electron diamagnetic drift (assuming $\partial p/\partial r < 0$) while a negative potential radial gradient leads to $\varOmega_{E\times B} < 0$ and a cross-field drift in the ion diamagnetic drift.

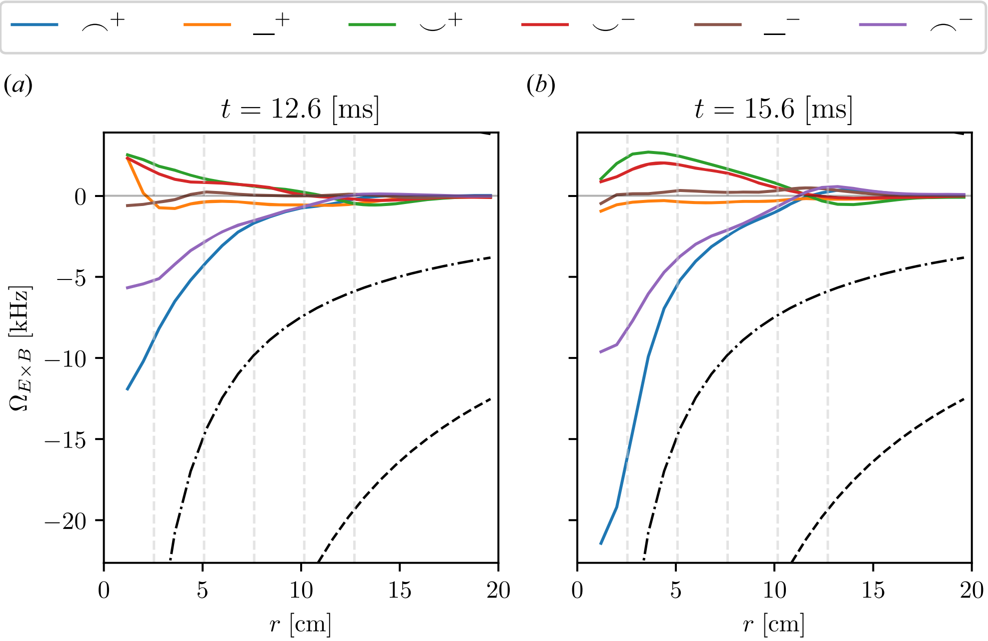

FIGURE 12. Angular plasma frequency on port #34, that is approximately 30 cm away from the multidisk electrode, at $t = 12.6$ ms (*a*) and $t = 15.6$ ms (*b*) for the six biasing scenarios (colour code) listed in table 2. Rotation is computed from the plasma potential profiles assuming pure $\boldsymbol{E} \times \boldsymbol{B}$ rotation. The dashed and dash–dotted black curves represent sonic rotation for $T_i = 5$ and 0.5 eV, respectively. The vertical grey dashed lines show the electrodes position.

Comparing these two contributions, one finds

$$\frac{\Omega_{E\times B}}{\Omega_D} = \frac{e}{kT}\frac{\partial \phi_p}{\partial r} \Big/ \left[\frac{1}{T}\frac{\partial T}{\partial r} + \frac{1}{n}\frac{\partial n}{\partial r}\right] \tag{6.3}$$

where ϕ_p, n and T are all functions of r. This shows that the $\boldsymbol{E} \times \boldsymbol{B}$ contribution dominates over the diamagnetic contribution if the drop in plasma potential over the characteristic gradient lengths for the density and the temperature is equal or larger than a few T_e. Because we observe radial voltage drops as large as 2 to $3T_e$ across the radius of the multidisk electrode while the density and temperature vary by at most 30 % in this same region, this assumption appears justified here, at least in the central region.

Under this simplifying assumption, it is possible to infer rotation from the plasma potential profiles measured for the different biasing scenarios. To do so we fit the plasma potential profiles using cubic smoothing splines, then fold back the negative x over the positive x to obtain an average radial profile $\phi_p(r) = [\phi_p(x = -r < 0) + \phi_p(x = r > 0)]/2$, which is finally differentiated with respect to r to get minus the radial electric field. The results obtained for active biasing in the main discharge ($t = 12.6$ ms) and in the early afterglow ($t = 15.6$ ms) are shown in figure 12.

As anticipated from the plasma potential profiles, we find the largest rotation in the core for the two negative gradient biasing scenarios (blue and purple) for which electrons are drawn by the electrodes on the axis. Rotation is anticlockwise, which is in the ion diamagnetic direction. Although the ion temperature was not directly measured in this experimental campaign, data obtained for comparable operating conditions suggest a typical value $0.5 \leq T_i \leq 5$ eV (Gekelman *et al.* 2016). Using these estimates as a baseline, figure 12 shows that the azimuthal drift remains subsonic, though it can locally approach what would be the sonic speed for the lower end of the ion temperature range. We also confirm that $\varOmega_{E\times B}$ remains at least two orders of magnitude smaller than the ion cyclotron frequency $\varOmega_{ci}$, supporting the fact that inertia corrections to the drift motion (Brillouin 1945) and perpendicular transport (Rax *et al.* 2015) are small. We further verify that the non-monotonic plasma potential profiles measured for the two positive gradient biasing scenarios (green and red) lead to a rotation reversal near the edge of the outermost electrode. Rotation is in this case clockwise in the core, and anticlockwise in the outer region. Finally, uniform biasing profiles (orange and brown), which we have seen lead to comparatively flat plasma potential profiles, consistently yield weak rotation.

Note, however, again that this analysis assumed $|\varOmega_{E\times B}| \gg |\varOmega_D|$. Clearly this is not valid for non-monotonic profiles near the point of reversal, where by definition $\varOmega_{E\times B} \sim 0$. This ordering is also questionable for flat potential profiles. In short, the examination of the potential profiles points to a strong plasma rotation driven by biasing for the negative gradient biasing scenarios, but a more in-depth analysis of the rotating equilibrium is called for other biasing scenarios.

6.2. *Discussion*

Having underlined the possibility to produce rapidly rotating plasmas via end-electrodes biasing, we now briefly discuss this result in light of related experiments previously conducted in LAPD. Of particular interest here is the work by Maggs, Carter & Taylor (2007) and Carter & Maggs (2009) in which a section of the chamber wall was biased positively with respect to the cathode to drive rotation.

An interesting observation is that although both biasing schemes may lead (did lead in the case of Maggs *et al.* (2007)) to rotation, they do so in very different ways. In the experiment discussed here, we surmised that rotation results from axial currents drawn by end electrodes, which then support a radial electric field. In this case, we have seen that rapid rotation appears more easily achievable in the anticlockwise direction ($E_r > 0$). On the other hand, in Maggs *et al.* (2007) it is an inward ion radial current driven by a radial voltage difference that led to a clockwise ($E_r < 0$) plasma rotation. Biasing the chamber negatively compared with the cathode, which would have led to anticlockwise rotation, was tried but shown to result in arcing. These basic differences are then expected to lead to distinct behaviours, which future studies may be able to examine.

First, the axial voltage drop model proposed here to explain end-electrodes biasing results would lead to a radial electric field that varies along z, decreasing in amplitude from the multidisk electrode to the anode. The corresponding axially dependent cross-field rotation would in turn translate into a twist of the plasma. On the contrary, the edge biasing, if done over the entire length of the plasma column, would in principle lead to an axially uniform rotation. Second, with end-biasing, the axial voltage drop and thus the radial electric field amplitude scale with the parallel Spitzer resistivity (5.1). Meanwhile, in edge biasing experiments ions are transported radially due to ion–neutral collisions, and the radial electric field is hence inversely proportional to the ion-driven Pedersen conductivity

$$\sigma_p = \frac{n_e m_i \nu_{in}}{{B_0}^2} \tag{6.4}$$

with ν_{in} the ion–neutral collision frequency. Comparing these two scaling, one expects completely different dependencies on plasma parameters.

Lastly, an important finding from Maggs *et al.* (2007) was that rotation driven by biasing led to a modification of transport properties, and more specifically to a reduction of cross-field transport from Bohm to classical rates, which translated into a steepening of the plasma density radial profiles. Although this is not the focus of our study, we note here in contrast looking back at figure 9 that there does not appear to be a noticeable change in density profile in the end-electrodes biasing results reported here.

7. Conclusion

An experimental campaign was carried out on the LAPD at the University of California, Los Angeles to study how biased end-electrodes can be used to control the radial potential profiles in the plasma bulk in the machine. It uses a set of five independently biased disk electrodes to control and impose boundary conditions for the potential approximately 11 m from the anode. Typical operating conditions in the main discharge were $n_e = 5 \times 10^{18}\ \mathrm{m}^{-3}$ and $T_e = 6 - 8$ eV.

Under these conditions, we observed that biasing has a very noticeable effect on the plasma potential in the machine, at least up to 6 m from the electrodes, with shifts in plasma potential that are comparable to the ± 30 V amplitude bias imposed on the electrodes. Examining the plasma response to non-uniform (though monotonic) biasing profiles, it was found that concave-down biasing profiles lead to the largest radial drops in plasma potential, no matter whether the applied bias is positive or negative. On the other hand, concave-up biasing profiles were shown to lead to non-monotonic profiles and less pronounced plasma potential radial gradients.

Analysing these results, it was shown that the radial profile of plasma potential in the machine is governed by the current drawn by each of the concentric electrodes and the axial resistance associated with Spitzer conductivity. This is consistent with the fact that $L/a\sqrt{\sigma_\perp/\sigma_\parallel} \ll 1$ for the operating conditions used here and the dimensions of LAPD. The largest radial variations observed for concave-down biasing profiles are notably driven by the larger electron current drawn by the on-axis electrode in this case, suggesting that steeper profiles may be achievable if drawing suitable parallel currents. These larger electron currents are, however, associated with plasma depletion on the magnetic field lines connected to the most positive electrode. It was also found that the nature of the plasma source on LAPD, namely the injection of energetic electrons through the anode, further imposes constraints between the plasma potential and the anode potential, which in turn forces the anode potential to track variations in plasma potential.

Finally, we computed the cross-field rotation expected from the different plasma potential profiles resulting from the various biasing scenarios. This analysis suggests that concave-down biasing profiles on end-electrodes may be used to produce rotating plasmas that locally approach sonic rotation, complementing other biasing-driven rotation techniques that had been previously demonstrated on LAPD. On the other hand, in producing non-monotonic potential profiles, concave-up biasing profiles would lead to flow reversal. In this latter case, though, one expects diamagnetic contributions to modify this picture.

Acknowledgements

The authors would like to thank P. Pribyl for his guidance on pulser biasing and emissive probes, V. Murinov for his help developing a script to extract electron temperature data from Langmuir scans, as well as Z. Lucky, M. Drandell and T. Ly for their technical support and assistance. The authors would also like to thank T. Carter and S. Vincena for constructive discussions of the experimental results, and S.J. Zweben for his help designing this experiment.

Editor H. Zohm thanks the referees for their advice in evaluating this article.

Funding

This research was performed at the Basic Plasma Science Facility at UCLA, which is funded by the USA Department of Energy and the National Science Foundation. R.G. gratefully acknowledges financial support for travel expenses from the International Action Program from CNRS INSIS.

Declaration of interests

The authors report no conflict of interest.

REFERENCES

Borisevich, V., Potanin, E. & Whichello, J.V. 2020 Plasma centrifuge with crossed $E \times B$ fields and thermally driven countercurrent flow. *IEEE Trans. Plasma. Sci.* **48** (10), 3472–3478.

Brillouin, L. 1945 A theorem of larmor and its importance for electrons in magnetic fields. *Phys. Rev.* **67** (7–8), 260–266.

Carter, T.A. & Maggs, J.E. 2009 Modifications of turbulence and turbulent transport associated with a bias-induced confinement transition in the large plasma device. *Phys. Plasmas* **16** (1).

Désangles, V., Bousselin, G., Poyé, A. & Plihon, N. 2021 Rotation and shear control of a weakly magnetized plasma column using current injection by emissive electrodes. *J. Plasma Phys.* **87** (3), 905870308.

Ellis, R.F., Case, A., Elton, R., Ghosh, J., Griem, H., Hassam, A., Lunsford, R., Messer, S. & Teodorescu, C. 2005 Steady supersonically rotating plasmas in the Maryland centrifugal experiment. *Phys. Plasmas* **12** (5).

Ellis, R.F., Hassam, A.B., Messer, S. & Osborn, B.R. 2001 An experiment to test centrifugal confinement for fusion. *Phys. Plasmas* **8** (5), 2057–2065.

Endrizzi, D., Anderson, J.K., Brown, M., Egedal, J., Geiger, B., Harvey, R.W., Ialovega, M., Kirch, J., Peterson, E., Petrov, Y.V., *et al.* 2023 Physics basis for the Wisconsin HTS axisymmetric mirror (WHAM). *J. Plasma Phys.* **89** (5), 975890501.

Fetterman, A.J. & Fisch, N.J. 2009 Wave-driven countercurrent plasma centrifuge. *Plasma Sources Sci. Technol.* **18** (4), 045003.

Fetterman, A.J. & Fisch, N.J. 2011 The magnetic centrifugal mass filter. *Phys. Plasmas* **18** (9), 094503–3.

Flanagan, K., Milhone, J., Egedal, J., Endrizzi, D., Olson, J., Peterson, E.E., Sassella, R. & Forest, C.B. 2020 Weakly magnetized, hall dominated plasma Couette flow. *Phys. Rev. Lett.* **125** (13), 135001.

Gekelman, W., Pribyl, P., Lucky, Z., Drandell, M., Leneman, D., Maggs, J., Vincena, S., Van Compernolle, B., Tripathi, S.K.P., Morales, G., *et al.* 2016 The upgraded large plasma device, a machine for studying frontier basic plasma physics. *Rev. Sci. Instrum.* **87** (2), 025105.

Gilmore, M., Hayes, T.R., Xie, S. & Yan, L. 2011 Flow profile changes and fluctuation suppression in a large scale helicon plasma with electrode biasing. In *Proceedings of the 38th EPS Conference on Plasma Physics*.

Gilmore, M., Lynn, A.G., Desjardins, T.R., Zhang, Y., Watts, C., Hsu, S.C., Betts, S., Kelly, R. & Schamiloglu, E. 2014 The HelCat basic plasma science device. *J. Plasma Phys.* **81** (1), 345810104.

Godyak, V.A. & Alexandrovich, B.M. 2015 Comparative analyses of plasma probe diagnostics techniques. *J. Appl. Phys.* **118** (23), 233302.

Gueroult, R., Evans, E.S., Zweben, S.J., Fisch, N.J. & Levinton, F. 2016 Initial experimental test of a helicon plasma based mass filter. *cces Sci. Technol.* **25** (3), 035024.

Gueroult, R., Rax, J.-M. & Fisch, N.J. 2014 The double well mass filter. *Phys. Plasmas* **21** (2), 020701.

Gueroult, R., Rax, J.-M. & Fisch, N.J. 2019*a* A necessary condition for perpendicular electric field control in magnetized plasmas. *Phys. Plasmas* **26** (12), 122106.

GUEROULT, R., RAX, J.-M. & FISCH, N.J. 2023 Wave propagation in rotating magnetised plasmas. *Plasma Phys. Control. Fusion* **65** (3), 034006.

GUEROULT, R., RAX, J.-M., ZWEBEN, S. & FISCH, N.J. 2018 Harnessing mass differential confinement effects in magnetized rotating plasmas to address new separation needs. *Plasma Phys. Control. Fusion* **60**, 014018.

GUEROULT, R., SHI, Y., RAX, J.-M. & FISCH, N.J. 2019*b* Determining the rotation direction in pulsars. *Nat. Commun.* **10** (1), 3232.

GUEROULT, R., ZWEBEN, S.J., FISCH, N.J. & RAX, J.-M. 2019*c* $E \times B$ configurations for high-throughput plasma mass separation: an outlook on possibilities and challenges. *Phys. Plasmas* **26** (4), 043511.

JIN, S., POULOS, M.J., COMPERNOLLE, B.V. & MORALES, G.J. 2019 Plasma flows generated by an annular thermionic cathode in a large magnetized plasma. *Phys. Plasmas* **26** (2), 022105.

KOEPKE, M.E., FINNEGAN, S.M., VINCENA, S., KNUDSEN, D.J. & CHASTON, C. 2008 Integrated campaign to study the stationary inertial Alfvén wave in the laboratory and space regimes. *Plasma Phys. Control. Fusion* **50** (7), 074004.

KOEPKE, M.E., FINNEGAN, S.M., VINCENA, S., KNUDSEN, D.J., NOGAMI, S.H. & VASSILIADIS, D. 2016 Laboratory evidence for stationary inertial Alfvén waves. *Plasma Phys. Control. Fusion* **58** (8), 084006.

KRISHNAN, M., GEVA, M. & HIRSHFIELD, J.L. 1981 Plasma centrifuge. *Phys. Rev. Lett.* **46** (1), 36–38.

LEHNERT, B. 1970 A partially ionized plasma centrifuge. *Phys. Scr.* **2** (3), 106.

LEHNERT, B. 1971 Rotating plasmas. *Nucl. Fusion* **11** (5), 485.

LEHNERT, B. 1973 The partially ionized plasma centrifuge. *Phys. Scr.* **7** (3), 102.

LIZIAKIN, G.D., ANTONOV, N.N., VORONA, N.A., GAVRIKOV, A.V., KISLENKO, S.A., KUZMICHEV, S.D., MELNIKOV, A.D., OILER, A.P., SMIRNOV, V.P., TIMIRKHANOV, R.A., *et al.* 2022 On the concept of plasma mass-separation in crossed $E \times B$ fields with a potential well (a review). *Plasma Phys Rep* **48** (11), 1251–1260.

LIZIAKIN, G.D., GAVRIKOV, A.V., USMANOV, R.A. & SMIRNOV, V.P. 2019 The electric field of the electrodes immersed into the rotating plasmas. *J. Phys.: Conf. Ser.* **1147**, 012130.

MAGGS, J.E., CARTER, T.A. & TAYLOR, R.J. 2007 Transition from Bohm to classical diffusion due to edge rotation of a cylindrical plasma. *Phys. Plasmas* **14** (5).

MARTIN, M.J., BONDE, J., GEKELMAN, W. & PRIBYL, P. 2015 A resistively heated CeB_6 emissive probe. *Rev. Sci. Instrum.* **86** (5), 053507.

NAGAOKA, K., OKAMOTO, A., YOSHIMURA, S., KONO, M. & TANAKA, M.Y. 2002 Spontaneous formation of a plasma hole in a rotating magnetized plasma: a giant burgers vortex in a compressible fluid. *Phys. Rev. Lett.* **89** (7), 075001.

OHKAWA, T. & MILLER, R.L. 2002 Band gap ion mass filter. *Phys. Plasmas* **9** (12), 5116–5120.

POULOS, M.J. 2019 Model for the operation of an emissive cathode in a large magnetized-plasma. *Phys. Plasmas* **26** (2), 022104.

PUTVINSKII, S.V. 1981 Plasma rotation caused by neutral injection. *Sov. J. Plasma Phys.* **7**, 547.

QIAN, Y., GEKELMAN, W., PRIBYL, P., SKETCHLEY, T., TRIPATHI, S., LUCKY, Z., DRANDELL, M., VINCENA, S., LOOK, T., TRAVIS, P., *et al.* 2023 Design of the lanthanum hexaboride based plasma source for the large plasma device at UCLA. *Rev. Sci. Instrum.* **94** (8), 085104.

RAX, J.M., FRUCHTMAN, A., GUEROULT, R. & FISCH, N.J. 2015 Breakdown of the Brillouin limit and classical fluxes in rotating collisional plasmas. *Phys. Plasmas* **22** (9), 092101.

RAX, J.M., GUEROULT, R. & FISCH, N.J. 2017 Efficiency of wave-driven rigid body rotation toroidal confinement. *Phys. Plasmas* **24** (3), 032504.

RAX, J.-M., GUEROULT, R. & FISCH, N.J. 2023 DC electric field generation and distribution in magnetized plasmas. *Phys. Plasmas* **30** (7), 072509.

ROMERO-TALAMÁS, C., ABEL, I., BALL, J., BASU, D., BEAUDOIN, B., DORSEY, L., ESCHBACH, N., HASSAM, A., KOETH, T., SHORT, Z., *et al.* 2021 Overview of the centrifugal mirror fusion experiment (CMFX). In *APS Division of Plasma Physics Meeting Abstracts*, APS Meeting Abstracts, vol. 2021, p. TP11.062.

SCHAFFNER, D.A., CARTER, T.A, ROSSI, G.D., GUICE, D.S., MAGGS, J.E., VINCENA, S. & FRIEDMAN, B. 2012 Modification of turbulent transport with continuous variation of flow shear in the large plasma device. *Phys. Rev. Lett.* **109** (13), 135002.

TANAKA, M.Y. 2019 Vortex in plasma. *Rev. Mod. Plasma Phys.* **3** (1).

TROTABAS, B. & GUEROULT, R. 2022 Trade-off in perpendicular electric field control using negatively biased emissive end-electrodes. *Plasma Sources Sci. Technol.* **31**, 025001.

VALENZUELA-VILLASECA, V., SUTTLE, L.G., SUZUKI-VIDAL, F., HALLIDAY, J.W.D., MERLINI, S., RUSSELL, D.R., TUBMAN, E.R., HARE, J.D., CHITTENDEN, J.P., KOEPKE, M.E., *et al.* 2023 Characterization of quasi-keplerian, differentially rotating, free-boundary laboratory plasmas. *Phys. Rev. Lett.* **130** (19), 195101.

WEYNANTS, R.R. & OOST, G.V. 1993 Edge biasing in tokamaks. *Plasma Phys. Control. Fusion* **35** (SB), B177–B189.

ZHANG, Q., SHI, P., LIU, M., LIN, M. & SUN, X. 2015 Electrode biasing experiment in kmax tandem mirror. *Fusion Sci. Technol.* **68** (1), 50–55.

ZWEBEN, S.J., GUEROULT, R. & FISCH, N.J. 2018 Plasma mass separation. *Phys. Plasmas* **25** (9), 090901.